Structural and Multidisciplinary Optimization (2024) 67:145
https://doi.org/10.1007/s00158-024-03869-w

RESEARCH PAPER

A concurrent optimization method of compliant structures embedded with movable piezoelectric actuators considering fundamental frequency constraints

Mingze Wang[1] · **Jingyu Hu**[1] · **Yunfeng Luo**[2] · **Shutian Liu**[1]

Received: 11 April 2024 / Revised: 4 June 2024 / Accepted: 2 August 2024 / Published online: 14 August 2024

Abstract

Compliant mechanisms with embedded piezoelectric actuators have widely been used in high vibration environments, which brings a requirement that the fundamental frequency should be greater than the external excitation frequency to avoid resonance. Existing topology optimization methods focus on enhancing the output stroke of compliant mechanisms while ignoring their dynamic properties. Hence, this work presents a concurrent optimization method of compliant structures embedded with movable piezoelectric actuators considering both the output stroke and dynamic properties. A density-based material interpolation scheme is developed to represent material properties in different sub-domains occupied by compliant mechanisms or actuators, and the topology of host compliant mechanisms and position of actuators are optimized simultaneously through designing the density field and geometric variables. To enhance dynamic properties of the mechanism, the fundamental frequency constraint is introduced into the standard compliant mechanism optimization formulation, in which the objective function is output displacement, and the constraint is volume fraction. The p-norm approximation function is adopted to alleviate the non-differentiability arising from the repeated eigenvalues and mode switching during the iterative process. Furthermore, using the adjoint method, the sensitivities of the objective function and constraints with respect to design variables are derived for the gradient-based optimizer. Several numerical examples are investigated to verify the effectiveness of the proposed optimization method and demonstrate the influence of the fundamental frequency constraints on the optimized results. The topologic results illustrate that the proposed method can attain a reasonable design, in which the output stroke is maximized and the fundamental frequency constraint is satisfied.

Keywords Concurrent optimization design · Compliant mechanisms · Piezoelectric actuators · Fundamental frequency constraint

1 Introduction

Due to the advantage of compact size and high energy density, piezoelectric actuators have widely been used in aerospace engineering (Mallick et al. 2014; Sun et al. 2016), high precision positioning (Moore et al. 2021; Shi et al. 2022), optical scanning (Wang et al. 2019; Schmerbauch et al. 2020), and so on. However, the maximum output stroke of the PSA is only 0.1% of its length, which cannot meet the desirable motion requirement of most application scenarios. To solve this issue, the maximum output displacement design of compliant mechanisms embedded with piezoelectric actuators has attracted significant attention from researchers and engineers.

In recent decades, several approaches have been developed to systematically design compliant mechanisms, such as the kinematics-based approach (Lobontiu and Garcia 2003; Ling 2019; Wang et al. 2023; Lai et al. 2023) and the topology optimization approach (Sigmund 1997; Nishiwaki et al. 1998; Wang et al. 2005; Li et al. 2021; Gao et al. 2023). Compared to conventional design methods, topology optimization allows for the exploration of the optimal material

---

Responsible editor: Zhen Luo

✉ Shutian Liu
stliu@dlut.edu.cn

[1] State Key Laboratory of Structural Analysis, Optimization and CAE Software for Industrial Equipment, Dalian University of Technology, Dalian 116024, China

[2] School of Mechanical Engineering, Shandong University, Jinan 250100, China

distribution without relying on intuition or design experience, which significantly enhances the design space. Since the pioneering work of Bendsøe and Kikuchi (1988), various topology optimization methods have been developed, such as the Solid Isotropic Material Penalty (SIMP) method (Clark et al. 2018; da Silva et al. 2019; Hu et al. 2024a), Bi-directional Evolutionary Structural Optimization (BESO) (Huang and Xie 2007; Teimouri and Asgari 2019; Lopes et al. 2021), Level set method (Wang et al. 2003; Allaire et al. 2004; Zhu and Zhang 2012; Van Dijk et al. 2013), and explicit feature-driven optimization method (Guo et al. 2014; Hoang and Jang 2017; Zhang et al. 2020; Zhu et al. 2021).

Based on proposed topology optimization methods, Sigmund (1997) first studied the topology optimization problem of the compliant mechanisms using the SIMP method, the mechanical advantage (MA) was considered as the objective function in his research. Nishiwaki et al. (1998) proposed a multi-objective optimization problem using the homogenization method as an application of compliant mechanism design, the objective function of which is a linear weighted combination formulation of the mutual potential energy (MPE) and strain energy (SE). Ansola et al. (2007) presented a topology optimization framework based on the BESO method for its application in designing compliant mechanisms, in which the ratio of the MPE and strain energy SE was used as the objective function to balance the output deformation and stiffness. It is noted that different optimization objectives are used in these studies, which aim to simultaneously consider the flexibility and stiffness of the mechanisms. Nowadays, the output displacement has become the most commonly used objective function for designing the compliant mechanisms, and the spring is arranged to the input and output port to simulate the interaction between the mechanisms and external objects (Pedersen et al. 2001; da Silva et al. 2019; Liu et al. 2020).

In the above works, compliant mechanisms are optimized under the assumption that the actuators are fixed in a predefined location and modeled with a specific spring stiffness and excitation force. This assumption constrains the design space and ignores the mechanical–electric coupling effect of the piezo-embedded compliant mechanisms. To find a better design of the piezo-embedded compliant mechanisms, it is necessary to take the inherent multi-physics characteristics of piezo-embedded compliant mechanisms into consideration and simultaneously optimize the layout of piezoelectric actuators and the topology of the host compliant structure. Based on the conventional SIMP method, Kögl and Silva (2005) proposed a piezoelectric material with penalization and polarization (PEMAP-P) model, which can simultaneously optimize the topology and polarization of the piezoelectric plate and shell actuators. Luo et al. (2009, 2010) developed a multiphase level set optimization method for integrated design of the host elastic materials and piezoelectric materials. Gao et al. (2022) introduced a robust isogeometric topology optimization method (RITO) for the design of piezoelectric actuators, which can achieve the optimization of the layout and polarization of piezoelectric actuators simultaneously.

Although the optimization of both piezoelectric actuators and elastic host structures has been addressed in the above studies, the layout of the piezoelectric actuators may result in a highly intricate geometry, posing challenges for manufacturing processes. To this end, several studies have been developed to optimize compliant mechanisms embedded with fixed-shape piezoelectric actuators. Wang et al. (2014) first proposed an integrated topology optimization framework to simultaneously design the topology of compliant host structures and the location of embedded actuators, in which the level set model and the independent point-wise density interpolation method are employed to describe the movements of actuators and topology of the host structure, respectively. Wang et al. (2022) further developed a hybrid topology optimization method for the integrated design of compliant mechanisms and piezoelectric actuators, which combines the projective transformation-based moving morphable components method and the parametric level set method (PMMC–PLS) to represent the layout of the embedded actuators and the host structure. Recently, Hu et al. (2024b) introduced a multi-material and multi-scale topology optimization method to further explore the design space of compliant structures with embedded movable piezoelectric actuators, where a density-based interpolation model that describes the piezoelectric actuators, multiple lattice materials of the host structure and their coating layer is proposed.

Most of the existing research focuses on optimizing the functional requirements of compliant mechanisms. Nevertheless, compliant structures embedded with piezoelectric actuators often operate in high vibration environments (Maddisetty and Frecker 2004; Zhu et al. 2020), neglecting the dynamic properties may lead to structural resonance

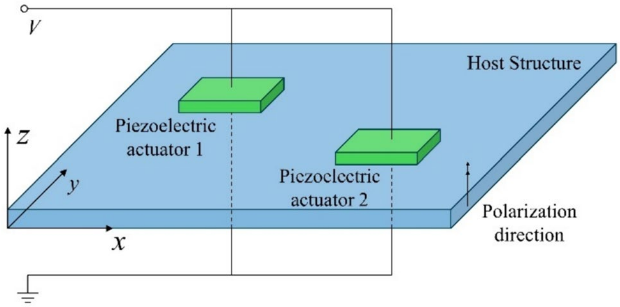

Fig. 1 Schematic diagram of the piezo-embedded compliant mechanism

and result in failure and damage. Therefore, it is necessary to develop a topology optimization method for compliant mechanisms that can simultaneously consider both their output displacement and dynamic properties. The primary challenges encountered in the dynamic topology optimization problem are the presence of repeated eigenvalues and mode switching during the iteration process, which pose difficulties for sensitivity analysis (Gravesen et al. 2011). Numerous authors presented alternatives to overcome the difficulties. Seyraniant et al. (1994) proposed a general multiparameter framework for sensitivity analysis of the single and repeated eigenvalues based on a mathematical perturbation technique. Ma et al. (1994) developed a mean-eigenvalue method, in which the weighted sum of the multiple eigenvalues is suggested as the objective function to overcome the differentiability issue. Du and Olhoff (2007) proposed an approach for the topology optimization method involving multiple eigenvalues based on a bound formulation, which can successfully alleviate the non-differentiable problem, but extra computations are required. Another validated approach to address the differentiability issue is to construct differentiable approximations of the eigenvalues (Torii and Faria 2017; Lopes et al. 2021; Li et al. 2023), such as the K–S function (Leader et al. 2019) and the p-norm function (Torii and Faria 2017; Quinteros et al. 2021). Despite the fact that dynamic topology optimization methods have been extensively developed in the past decades, the topology optimization method for piezo-actuated compliant mechanisms considering dynamic properties has not yet been investigated.

In this paper, a concurrent optimization method of compliant structures embedded with movable piezoelectric actuators considering fundamental frequency constraints is proposed, where the position of the embedded piezoelectric actuators and the topology of the host structure are simultaneously optimized. The objective of the optimization is to maximize the output displacement with considering the fundamental frequency constraint and the volume constraint. The SIMP-based computational framework is developed, in which the embedded actuators are described by a modified K–S function and projected into a density field to avoid remeshing the grid (Wang et al. 2020). To address the non-differentiability issue, an efficient p-norm approximation function for the fundamental frequency constraint is applied. The gradient-based optimizer is used to update the design variables and the sensitivities are computed using the adjoint method. Several numerical examples are investigated to validate the effectiveness of the proposed method.

The rest of this paper is organized as follows: Sect. 2 introduces the electro-mechanical finite element model and the topology representation scheme of the piezo-embedded compliant mechanism. After that, the topology optimization formulation and sensitivity analysis are presented in Sect. 3. In Sect. 4, three numerical examples are investigated to demonstrate the effectiveness of the proposed method. Finally, Sect. 5 gives the conclusions of this paper.

2 Finite element model and topology description of the piezo-embedded compliant mechanism

2.1 Finite element model

In this work, the electro-mechanical compliant mechanism is considered linear and in the plane stress state. The polarization direction of the piezoelectric actuators is parallel to the z-axis, as shown in Fig. 1. The constitutive equations of the piezo-embedded compliant mechanism can be written as

$$\begin{aligned} \boldsymbol{\sigma} &= \mathbf{D}\boldsymbol{\varepsilon} - \mathbf{e}\mathbf{E} \\ \mathbf{d}_E &= \mathbf{e}^T\boldsymbol{\varepsilon} + \boldsymbol{\kappa}\mathbf{E}^{,} \end{aligned} \tag{1}$$

where $\boldsymbol{\sigma}$ and $\boldsymbol{\varepsilon}$ represent the stress and strain vectors, respectively. $\mathbf{d}_E$ and $\mathbf{E}$ are the electric displacement vector and electric field vector, respectively. $\mathbf{D}$ denotes the elastic stiffness matrix, $\mathbf{e}$ is the piezoelectric constant matrix, and $\boldsymbol{\kappa}$ represents the matrix of permittivity in constant mechanical strain. It should be noted that only a uniform electric field distributed in the poling direction is considered in the above equation, namely $\mathbf{E} = \left\{ 0 \;\; 0 \;\; \phi/h \right\}^T$, where ϕ is the applied voltage and h is the plate thickness.

The mechanical balance equation in the absence of body load and the source-free Maxwell's equation of the piezo-embedded structure under the plane stress assumption can be written as

$$\begin{cases} \mathbf{A}\boldsymbol{\sigma} = \rho \dfrac{\partial^2 \mathbf{u}}{\partial t^2} \\ \nabla \mathbf{d}_E = 0 \end{cases}, \tag{2}$$

where $\mathbf{A}$ is the differential matrix defined as

$$A = \begin{bmatrix} \frac{\partial}{\partial x} & 0 & \frac{\partial}{\partial y} \\ 0 & \frac{\partial}{\partial y} & \frac{\partial}{\partial x} \end{bmatrix}. \tag{3}$$

$\mathbf{u}$ is the displacement vector and ∇ is the nabla operator. Neglecting the damping effect, the finite element formulation of Eq. (1) and Eq. (2) can be obtained using the Hamilton's variational principle

$$\begin{bmatrix} \mathbf{M} & \mathbf{0} \\ \mathbf{0} & \mathbf{0} \end{bmatrix} \begin{Bmatrix} \ddot{\mathbf{U}} \\ \ddot{\boldsymbol{\Phi}} \end{Bmatrix} + \begin{bmatrix} \mathbf{K}_{uu} & \mathbf{K}_{u\phi} \\ \mathbf{K}_{\phi u} & \mathbf{K}_{\phi\phi} \end{bmatrix} \begin{Bmatrix} \mathbf{U} \\ \boldsymbol{\Phi} \end{Bmatrix} = \begin{Bmatrix} \mathbf{F} \\ \mathbf{Q} \end{Bmatrix}, \tag{4}$$

where $\mathbf{M}$ is the mass matrix, $\mathbf{K}_{uu}$ is the mechanical stiffness matrix, $\mathbf{K}_{u\phi} = \mathbf{K}_{\phi u}$ is the piezoelectric coupling matrix, and

Fig. 2 Illustration of the non-overlap constraint for the embedded actuators

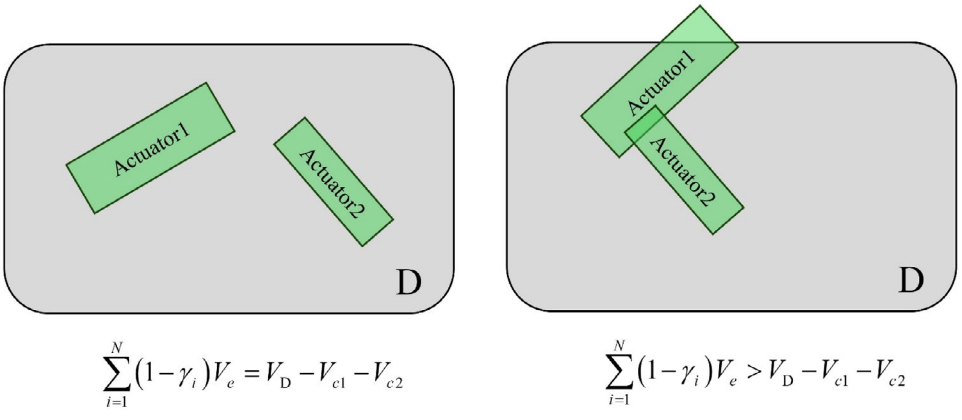

(a) (b)

$\mathbf{K}_{\phi\phi}$ denotes the dielectric matrix. $\mathbf{U}$ and $\mathbf{\Phi}$ are the nodal displacement vector and nodal electric potential vector, respectively. $\mathbf{F}$ is the force vector and $\mathbf{Q}$ is the nodal electric charge vector. Since piezoelectric components in this work only play the role of actuators, the finite element equation of the structure can be reduced to

$$\mathbf{M}\ddot{\mathbf{U}} + \mathbf{K}_{uu}\mathbf{U} + \mathbf{K}_{u\phi}\mathbf{\Phi} = \mathbf{0}. \tag{5}$$

The stiffness matrix and the piezoelectric coupling matrix of element e can be calculated by

$$\begin{aligned} \mathbf{K}_{uu}^{e} &= \int_{\Omega_e} \mathbf{B}_u^{\mathrm{T}}\mathbf{D}_e\mathbf{B}_u \mathrm{d}\Omega_e \\ \mathbf{K}_{u\phi}^{e} &= \int_{\Omega_e} \mathbf{B}_u^{\mathrm{T}}\mathbf{e}_e\mathbf{B}_\phi \mathrm{d}\Omega_e \end{aligned}, \tag{6}$$

where $\mathbf{B}_u$ and $\mathbf{B}_\phi$ are the displacement–strain and electric field–potential matrix, respectively. The mass matrix of element e can be expressed as

$$\mathbf{M}^e = \rho_e \int_{\Omega_e} \mathbf{N}^T\mathbf{N}\mathrm{d}\Omega_e, \tag{7}$$

where $\mathbf{N}$ is the matrix of the interpolation function and ρ_e denotes the material density of element e.

Since the magnitude of the element stiffness matrix $\mathbf{K}_{uu}^{e}$ is large compared to the piezoelectric coupling matrix $\mathbf{K}_{u\phi}^{e} = \mathbf{K}_{\phi u}^{e}$ and the dielectric matrix $\mathbf{K}_{\phi\phi}^{e}$, solving the Eq. (5) may face numerical instability (Homayouni-Amlashi et al. 2021). To this end, a normalization is performed as follows:

$$\begin{cases} \overline{\mathbf{K}}_{uu}^{e} = \mathbf{K}_{uu}^{e}/k_0 \\ \overline{\mathbf{K}}_{u\phi}^{e} = \mathbf{K}_{u\phi}^{e}/\alpha_0 \\ \overline{\mathbf{M}}^{e} = \mathbf{M}^{e}/m_0 \end{cases}, \tag{8}$$

where k_0, α_0, and m_0 are the largest absolute value of the three matrices. The normalized finite element equation can be written as

$$\overline{\mathbf{M}}\ddot{\overline{\mathbf{U}}} + \overline{\mathbf{K}}_{uu}\overline{\mathbf{U}} + \overline{\mathbf{K}}_{u\phi}\overline{\mathbf{\Phi}} = \overline{\mathbf{F}}, \tag{9}$$

in which the normalized displacement vector $\overline{\mathbf{U}}$ and electric potential vector $\overline{\mathbf{\Phi}}$ can be obtained as follows:

$$\begin{cases} \overline{\mathbf{U}} = k_0\mathbf{U} \\ \overline{\mathbf{\Phi}} = \alpha_0\mathbf{\Phi} \end{cases}. \tag{10}$$

2.2 Topology description of the embedded piezoelectric actuators

The i-th embedded piezoelectric actuator can be fully determined by its location parameters $\mathbf{c_i} = \left(x_i^0, y_i^0, \theta_i^0\right)$ and topology description function φ_i, where x_i^0 and y_i^0 are horizontal and vertical coordinates of the center of the i-th embedded piezoelectric actuator. θ_i^0 is the rotation angle relative to the horizontal. The topology description function φ_i can be described as follows:

$$\begin{cases} \varphi_i(\mathbf{x}) > 0, & \text{if } \mathbf{x} \notin \Omega_i \\ \varphi_i(\mathbf{x}) = 0, & \text{if } \mathbf{x} \in \partial\Omega_i \\ \varphi_i(\mathbf{x}) < 0, & \text{if } \mathbf{x} \in \Omega_i \end{cases}, \tag{11}$$

where $\mathbf{x}$ is the centroid coordinate vector of elements. Ω_i and $\partial\Omega_i$ denote the sub-domain of the i-th embedded actuators and its boundary, respectively.

For embedded actuators with fixed shapes, the topology description function φ_i can be reformulated as the function of location parameters

$$\varphi_i = \varphi_i\left(\overline{x}_i, \overline{y}_i\right), \tag{12}$$

where $(\bar{x}_i, \bar{y}_i)$ are local coordinates aligned with the x–y axes of the i-th embedded actuator

$$\begin{Bmatrix} \bar{x}_i \\ \bar{y}_i \end{Bmatrix} = \begin{bmatrix} \cos\theta_i^0 & \sin\theta_i^0 \\ -\sin\theta_i^0 & \cos\theta_i^0 \end{bmatrix} \begin{Bmatrix} x - x_i^0 \\ y - y_i^0 \end{Bmatrix}. \tag{13}$$

In this work, a density-based topology optimization framework is established. To this end, the geometry of embedded actuators is projected onto a [0 1] density field using the following Heaviside function:

$$\boldsymbol{\gamma} = 1 - \prod_{i=1}^{N_a} \frac{1}{1 + e^{-\beta\varphi_i(\mathbf{x})}}, \tag{14}$$

where β denotes the sharpness of the smoothed Heaviside function. N_a is the number of the embedded actuators. The elements of embedded piezoelectric actuators are defined by $\boldsymbol{\gamma} = 1$.

The presence of the host structure is described by the density vector $\boldsymbol{\zeta} = (\zeta_1, ..., \zeta_N)$, where N is the total number of the discrete elements.

2.3 Material interpolation scheme

Since the shape and location of the embedded actuators are described by a [0 1] density field $\boldsymbol{\gamma}$, the multi-component optimization problem can be regarded as a multi-material optimization problem. Thus, a multi-material interpolation scheme is presented to represent the elastic properties and the material density of the host structures and embedded actuators, which can be expressed as follows:

$$\mathbf{D}_e = \zeta_e^{p_1}\left(1 - \gamma_e^{p_1}\right)\mathbf{D}_h + \gamma_e^{p_1}\mathbf{D}_a, \tag{15}$$

$$\rho_e = \zeta_e^{q}\left(1 - \gamma_e^{q}\right)\rho_h + \gamma_e^{q}\rho_a, \tag{16}$$

where $\mathbf{D}_h$ and $\mathbf{D}_a$ denote the elastic stiffness matrix of the host structure and the embedded actuators, while ρ_h and ρ_a are the corresponding material density. p_1 and q are the penalization coefficients for the stiffness matrices and material density, respectively.

The stiffness matrix of the element e are determined by both density field $\boldsymbol{\zeta}$ and $\boldsymbol{\gamma}$. For $\gamma_e = 1$, that is, the element is located in one of the embedded actuators, we have $\mathbf{D}_e = \mathbf{D}_a$; for $\zeta_e = 1$ and $\gamma_e = 0$, that is, the element is inside the host structure, then $\mathbf{D}_e = \mathbf{D}_h$; and for $\zeta_e = 0$ and $\gamma_e = 0$, that is, the element is void, then $\mathbf{D}_e = 0$.

The piezoelectric constant matrix of the element e can be obtained as follows:

$$\mathbf{e}_e = \gamma_e^{p_2}\mathbf{e}_a, \tag{17}$$

where p_2 is the penalization coefficient for the piezoelectric constant matrix of the embedded actuators. $\mathbf{e}_a$ is the piezoelectric matrix of the selected piezoelectric material under plane stress assumption:

$$\mathbf{e}_a = \begin{bmatrix} e_{31} & e_{32} & 0 \end{bmatrix}^{\mathrm{T}}. \tag{18}$$

Substituting Eqs. (14)–(16) into Eqs. (5)–(6), the element stiffness matrix, the piezoelectric coupling matrix, and the mass matrix can be rewritten as

$$\begin{aligned} \mathbf{K}_{uu}^e &= \zeta_e^{p_1}\left(1 - \gamma_e^{p_1}\right)\mathbf{K}_{uuh}^e + \gamma_e^{p_1}\mathbf{K}_{uua}^e \\ \mathbf{K}_{u\phi}^e &= \gamma_e^{p_2}\mathbf{K}_{u\phi a}^e \\ \mathbf{M}^e &= \zeta_e^{q}\left(1 - \gamma_e^{q}\right)\mathbf{M}_h^e + \gamma_e^{q}\mathbf{M}_a^e \end{aligned}, \tag{19}$$

where the constant matrices corresponding to the solid material $\mathbf{K}_{uuh}^e$, $\mathbf{K}_{uua}^e$, $\mathbf{K}_{u\phi a}^e$, $\mathbf{M}_h^e$, and $\mathbf{M}_a^e$ can be obtained as

$$\begin{cases} \mathbf{K}_{uuh}^e = \int_{\Omega_e} \mathbf{B}_u^{\mathrm{T}}\mathbf{D}_{\mathbf{h}}\mathbf{B}_u \mathrm{d}\Omega_e \\ \mathbf{K}_{uua}^e = \int_{\Omega_e} \mathbf{B}_u^{\mathrm{T}}\mathbf{D}_{\mathbf{a}}\mathbf{B}_u \mathrm{d}\Omega_e \\ \mathbf{K}_{u\phi a}^e = \int_{\Omega_e} \mathbf{B}_u^{\mathrm{T}}\mathbf{e}_{\mathbf{a}}\mathbf{B}_u \mathrm{d}\Omega_e \\ \mathbf{M}_h^e = \rho_h \int_{\Omega_e} \mathbf{N}^T\mathbf{N}\mathrm{d}\Omega_e \\ \mathbf{M}_a^e = \rho_a \int_{\Omega_e} \mathbf{N}^T\mathbf{N}\mathrm{d}\Omega_e \end{cases}. \tag{20}$$

3 Topology optimization considering fundamental frequency constraints

3.1 Problem statement

In this paper, the topology optimization problem for maximizing the output displacement u_{out} with volume constraint and fundamental frequency constraints is considered. The mathematical formulation of the optimization problem can be expressed as

Table 1 Material properties of the piezoelectric actuators

Parameter	Value
Young's modulus E(GPa)	74
Poisson's ratio ν	0.3
Density ρ[kg/m^3]	7800
Piezoelectric constant e_{31}	– 9.3
Piezoelectric constant e_{32}	– 9.3

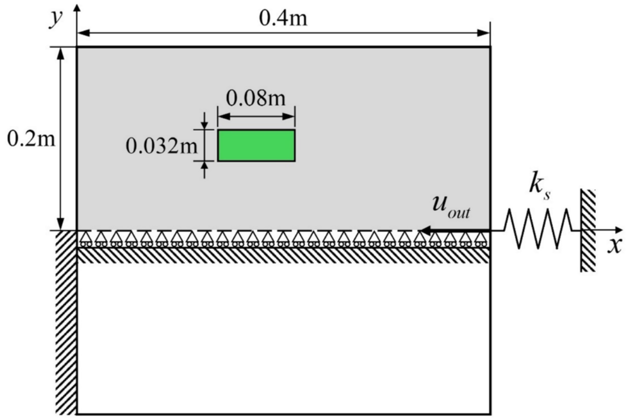

Fig. 3 Analysis domain and boundary conditions of the displacement inverting mechanism. The reduced design domain is highlighted in gray

$$
\begin{aligned}
&\text{Find:} \quad \begin{cases} \boldsymbol{\zeta} = (\zeta_1, \zeta_2, \dots, \zeta_N) \\ \mathbf{c} = (\mathbf{c}_1, \mathbf{c}_2, \dots \mathbf{c}_{\mathrm{N_a}}) \end{cases} \\
&\text{Max:} \quad u_{\text{out}} = \mathbf{L}^{\mathrm{T}} \overline{\mathbf{U}} \\
&\mathrm{S.t.}: \quad \overline{\mathbf{K}}_{uu} \overline{\mathbf{U}} + \overline{\mathbf{K}}_{u\phi} \overline{\boldsymbol{\Phi}} = \mathbf{0} \\
&\qquad g_1 = \sum_{i=1}^{N} \zeta_i V_i - f_1 V_{\mathrm{D}} \le 0\,, \quad (i = 1, 2, \dots, N) \qquad , \\
&\qquad g_2 = \sum_{i=1}^{N} (1 - \gamma_i) V_i \le V_{\mathrm{D}} - \sum_{j=1}^{N_a} V_{cj}\,, \quad (i = 1, 2, \dots, N) \\
&\qquad g_3 = \min(\omega_j) \ge \overline{\omega}\,, \quad (j = 1, \dots, J_0) \\
&\qquad 0 < \zeta_{\min} \le \zeta_e \le 1
\end{aligned} \tag{21}
$$

where $\boldsymbol{\zeta}$ denote the design variables of the host structure. **c** is the set of the location parameters associated with embedded actuators. **L** is a vector with the value of 1 at the degree of output end, and the rest entries of which are all zero. g_1 is

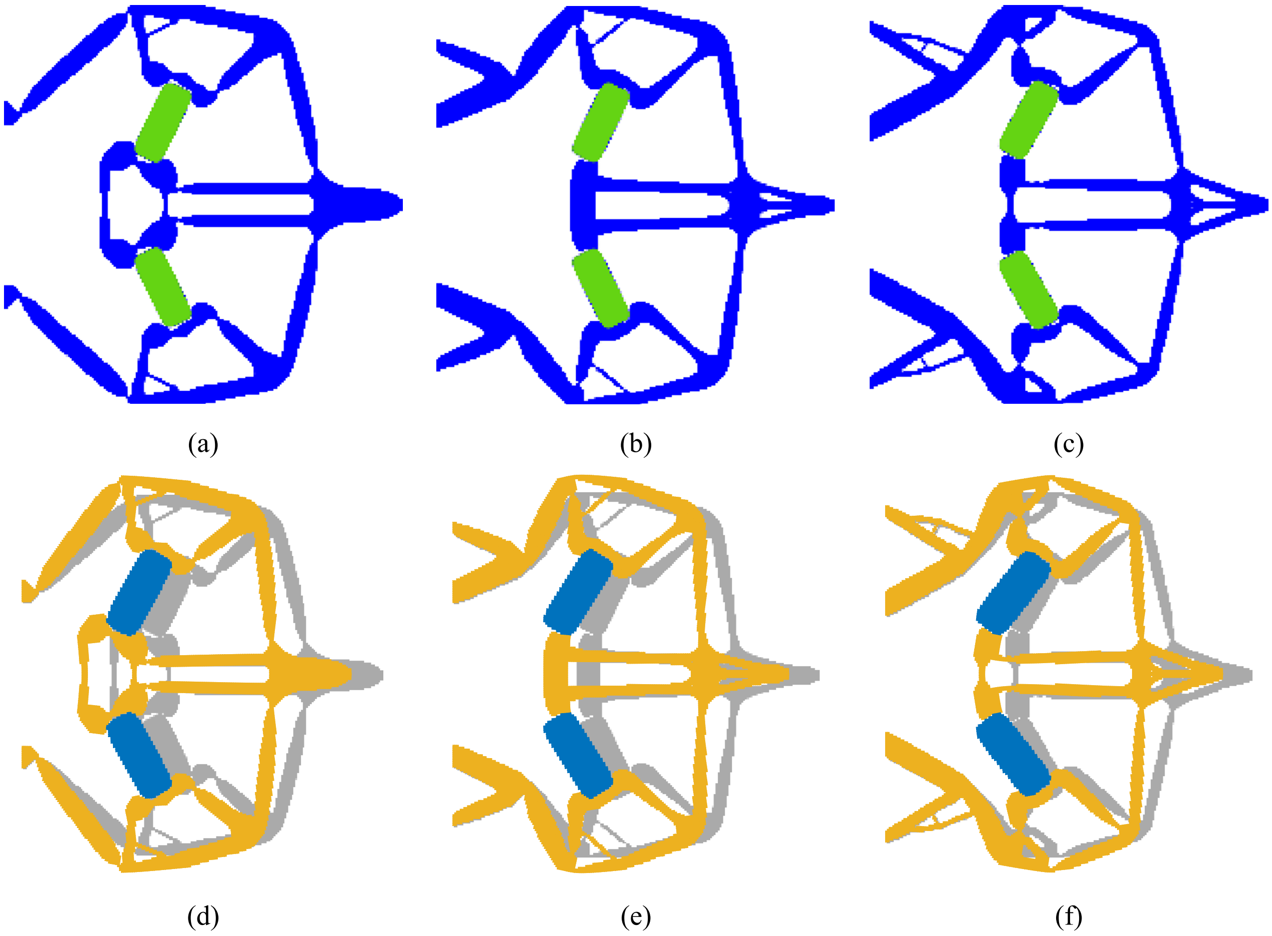
(a) (b) (c)

(d) (e) (f)

Fig. 4 Optimized topology of the displacement inverting mechanism: **a** without frequency constraint; **b** $\overline{\omega} = 200$ Hz; and **c** $\overline{\omega} = 300$ Hz . Deformation of the optimized designs: **d** without frequency constraint; **e** $\overline{\omega} = 200$ Hz; and **f** $\overline{\omega} = 300$ Hz

Table 2 Comparing the optimized results for different cases in example 1

	Optimal layout	$u_{\text{out}}(\mu m)$	ω_1(Hz)	ω_2(Hz)	ω_3(Hz)
No constraint	(0.1591 m, 0.1175 m, –1.1195 rad)	–10.452	33.48	478.42	589.12
$\overline{\omega} = 200$ Hz	(0.1651 m, 0.1168 m, –1.1120 rad)	–9.846	200.04	527.06	840.01
$\overline{\omega} = 300$ Hz	(0.1595 m, 0.1148 m, –1.0588 rad)	–9.452	300.30	649.15	826.63

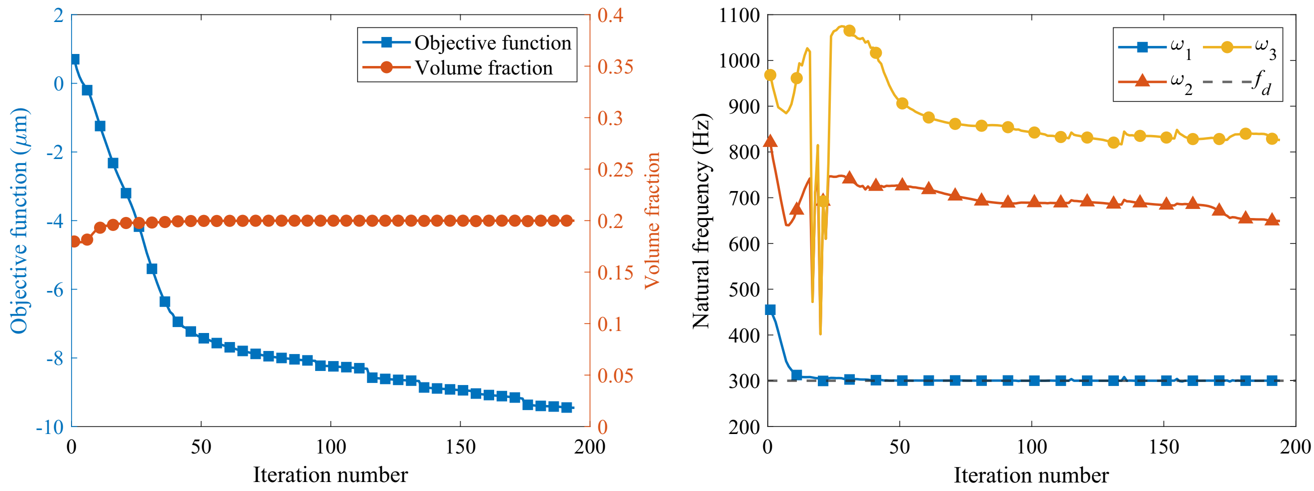

(a) (b)

Fig. 5 Iteration history for $\overline{\omega} = 300$ Hz case: **a** the objective function and volume fraction and **b** the first three eigenfrequencies

the volume constraint of the host structure, where V_i denotes the volume of the element i, V_{D} is the volume of the entire design domain, and f_1 represents the allowable volume fraction of the host structure. The non-overlap constraint of the embedded actuators is determined by g_2, where V_{cj} is the volume of j-th embedded actuator. To better understand, the basic idea of non-overlap constraint is illustrated in Fig. 2. g_3 denotes the fundamental frequency constraint. ω_j is the j-th natural frequency of the structure. $J_0 > 1$ is the number of natural frequencies used for evaluating the fundamental frequency. $\overline{\omega}$ is the lower bound of the fundamental frequency. A lower threshold $\zeta_{\min} = 0.001$ of design variables ζ_e is set to avoid numerical difficulties when optimization.

The natural frequencies of the structure can be obtained by solving the generalized eigenvalue problem

$$\mathbf{K}\boldsymbol{\eta}_i = \lambda_i \mathbf{M}\boldsymbol{\eta}_i, \tag{22}$$

where $\mathbf{K}$ and $\mathbf{M}$ are the global stiffness and mass matrix, respectively. For the embedded structure in this work, $\mathbf{K} = \mathbf{K}_{uu}$. λ_i is the i-th eigenvalue and $\boldsymbol{\eta}_i$ represents the corresponding eigenvector. It should be noted that to better calculate the sensitivity information of the eigenvalues, the eigenvectors are normalized with respect to the mass matrix $\mathbf{M}$

$$\boldsymbol{\eta}_i^{\mathrm{T}} \mathbf{M} \boldsymbol{\eta}_j = \delta_{ij}. \tag{23}$$

The p-norm approximation method has been adopted in this work to avoid difficulties related to sensitivity analysis.

$$g_3 = \left[\sum_{i=1}^{J_0} \frac{1}{\lambda_i^p} \right]^{-\frac{1}{p}} \geq \overline{\lambda}, \tag{24}$$

where $p = 8$ is used in this work for a smooth approximation of the minimum eigenvalue. $\overline{\lambda} = \left(2\pi\overline{\omega}\right)^2$ denote the lower bound of the minimum eigenvalue.

3.2 Sensitivity analysis

To update design variables using the gradient-based optimizer, the sensitivities of the objective function and constraints are obtained in this section. The sensitivity of the output displacement with respect to design variable s (ζ_i, $\mathbf{c}_i$) is calculated using the adjoint method:

$$\begin{aligned} \frac{\partial u_{out}}{\partial s} &= \frac{\partial}{\partial s}\left[\mathbf{L}^{\mathrm{T}}\overline{\mathbf{U}} + \boldsymbol{\lambda}^{\mathrm{T}}\left(\overline{\mathbf{K}}_{uu}\overline{\mathbf{U}} + \overline{\mathbf{K}}_{u\phi}\overline{\boldsymbol{\Phi}} \right) \right] \\ &= \left(\mathbf{L}^{\mathrm{T}} + \boldsymbol{\lambda}^{\mathrm{T}}\overline{\mathbf{K}}_{uu} \right)\frac{\partial \overline{\mathbf{U}}}{\partial s} + \boldsymbol{\lambda}^{\mathrm{T}}\frac{\partial \overline{\mathbf{K}}_{uu}}{\partial s}\overline{\mathbf{U}} + \boldsymbol{\lambda}^{\mathrm{T}}\frac{\partial \overline{\mathbf{K}}_{u\phi}}{\partial s}\overline{\boldsymbol{\Phi}} \end{aligned}, \tag{25}$$

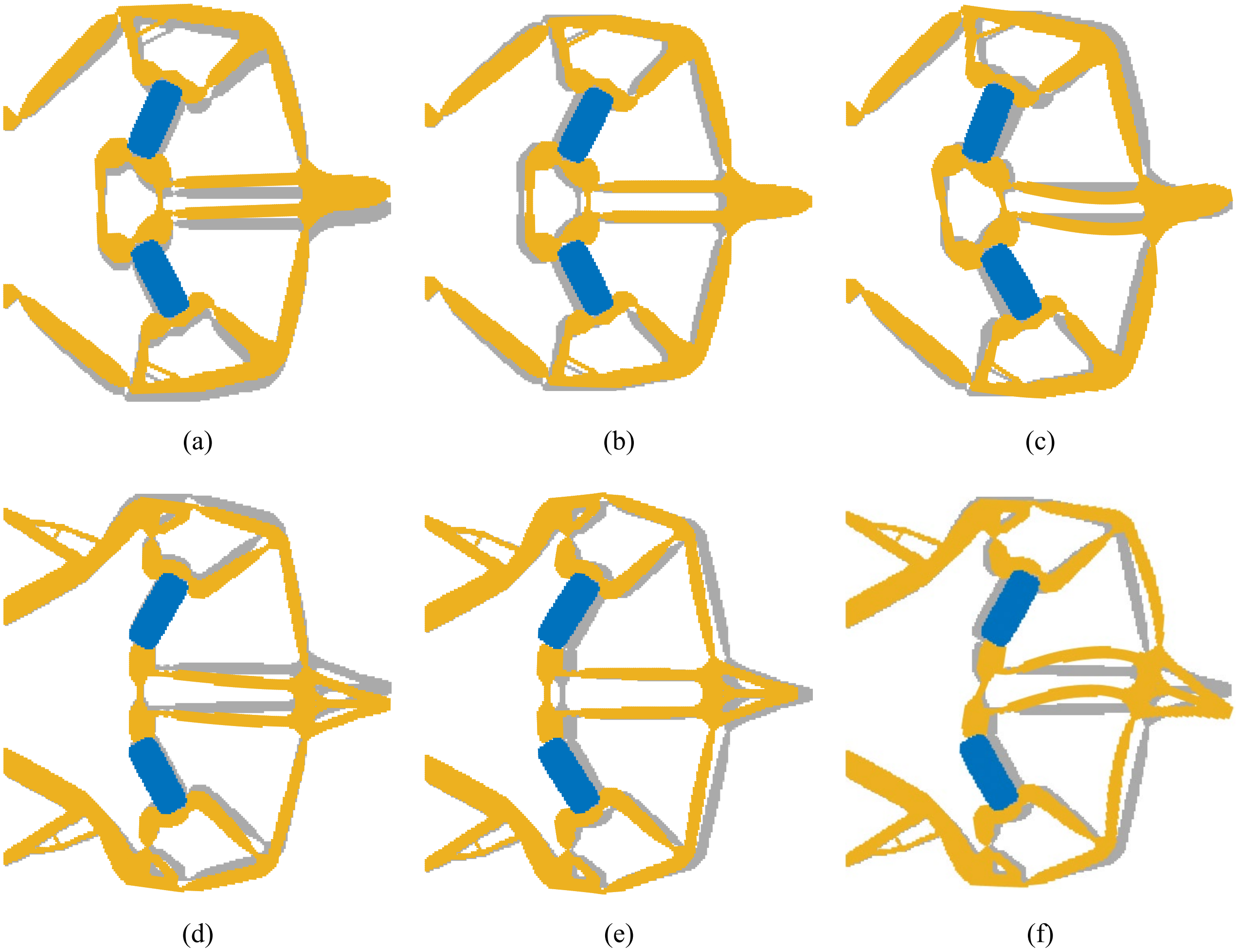
(a) (b) (c)

(d) (e) (f)

Fig. 6 The first three eigenmodes of the optimized design: **a**–**c** the first, second, and third eigenmode of the optimized design without frequency constraint; and **d**–**f** the first, second, and third eigenmode of the optimized design with frequency constraint $\overline{\omega} = 300$ Hz

where the adjoint vector $\boldsymbol{\lambda}$ is assigned as the solution of the equation $\overline{\mathbf{K}}_{uu}\boldsymbol{\lambda} = -\mathbf{L}$ such that the derivative term $\partial\overline{\mathbf{U}}/\partial s$ can be eliminated.

The derivative of the element stiffness matrix with respect to ζ_i can be calculated as

$$\frac{\partial \overline{\mathbf{K}}_{uu}^{e}}{\partial \zeta_i} = \frac{p_1 \zeta_e^{p_1-1}\left(1-\gamma_e^{p_1}\right)\mathbf{K}_{uuh}^{e}}{k_0}. \tag{26}$$

The derivative of the stiffness matrix and piezoelectric coupling matrix with respect to the location parameters $c_{ik} \in \left(x_i^0, y_i^0, \theta_i^0\right)$ of i-th embedded actuator can be calculated using the chain rule as follows:

$$\frac{\partial \overline{\mathbf{K}}_{uu}}{\partial c_{ik}} = \sum_{e=1}^{N} \frac{\partial \overline{\mathbf{K}}_{uu}^{e}}{\partial \gamma_e}\frac{\partial \gamma_e}{\partial \varphi_i}\frac{\partial \varphi_i}{\partial c_{ik}}, \tag{27}$$

$$\frac{\partial \overline{\mathbf{K}}_{u\phi}}{\partial c_{ik}} = \sum_{e=1}^{N} \frac{\partial \overline{\mathbf{K}}_{u\phi}^{e}}{\partial \gamma_e}\frac{\partial \gamma_e}{\partial \varphi_i}\frac{\partial \varphi_i}{\partial c_{ik}}, \tag{28}$$

where the derivative term $\partial\overline{\mathbf{K}}_{uu}^{e}/\partial\gamma_e$ and $\partial\overline{\mathbf{K}}_{u\phi}^{e}/\partial\gamma_e$ can be obtained by differentiating Eq. (15) with respect to γ_e

$$\frac{\partial \overline{\mathbf{K}}_{uu}^{e}}{\partial \gamma_e} = \frac{-p_1\zeta_e^{p_1}\gamma_e^{(p_1-1)}\mathbf{K}_{uuh}^{e} + p_1\gamma_e^{(p_1-1)}\mathbf{K}_{uua}^{e}}{k_0}, \tag{29}$$

$$\frac{\partial \overline{\mathbf{K}}_{u\phi}^{e}}{\partial \gamma_e} = \frac{p_2\gamma_e^{(p_2-1)}\mathbf{K}_{u\phi a}^{e}}{\alpha_0}. \tag{30}$$

The derivative term $\partial\gamma_e/\partial\varphi_i$ can be derived from Eq. (14) as

$$\frac{\partial \gamma_e}{\partial \varphi_i} = -\left(1-\gamma_e\right)\frac{\beta e^{-\beta\varphi_i}}{1+e^{-\beta\varphi_i}}. \tag{31}$$

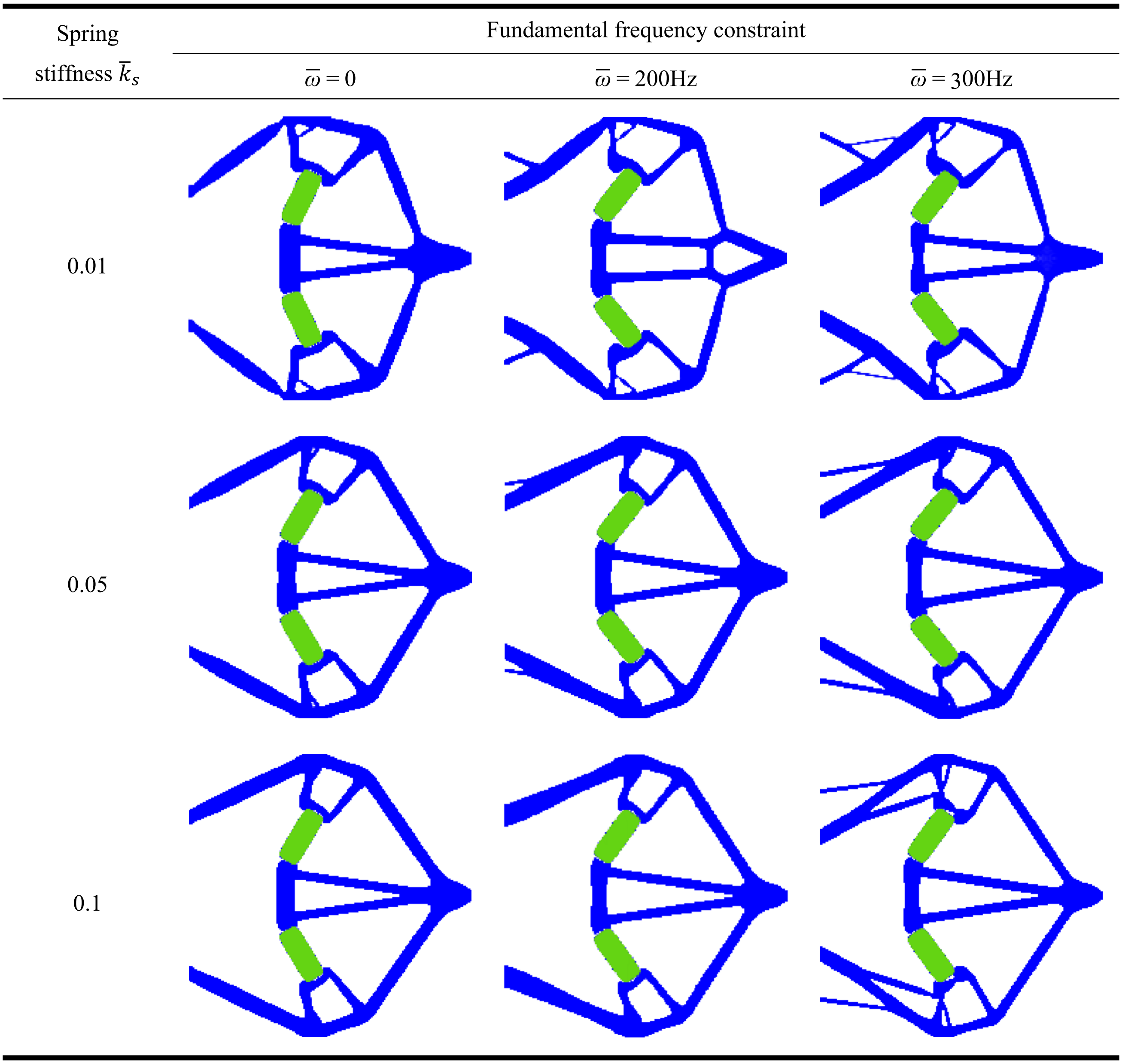

Fig. 7 Optimal results under different spring stiffnesses

Table 3 Optimized results under different spring stiffnesses

$\bar{k}_s$	$\bar{\omega}$(Hz)	Optimal layout	$u_{\text{out}}(\mu m)$	ω_1(Hz)
0.01	0	(0.1598 m, 0.1140 m, –1.1331 rad)	–7.171	63.61
	200	(0.1605 m, 0.1103 m, –0.9137 rad)	–6.805	200.04
	300	(0.1623 m, 0.1146 m, –0.9080 rad)	–6.621	300.12
0.05	0	(0.1593 m, 0.1145 m, –1.0342 rad)	–3.194	118.92
	200	(0.1639 m, 0.1154 m, –0.9047 rad)	–3.065	200.01
	300	(0.1616 m, 0.1107 m, –0.8863 rad)	–2.963	300.03
0.1	0	(0.1589 m, 0.1172 m, –1.0262 rad)	–2.006	141.33
	200	(0.1591 m, 0.1160 m, –0.9523 rad)	–1.964	200.10
	300	(0.1582 m, 0.1149 m, –0.9977 rad)	–1.932	300.02

In this paper, the rectangular embedded actuators are adopted. The topology description functions for the embedded actuators can be expressed as

$$\varphi_i = \left(\frac{\bar{x}_i}{a_i}\right)^6 + \left(\frac{\bar{y}_i}{b_i}\right)^6 - 1, \tag{32}$$

where a_i and b_i are the semi-major and semi-minor lengths of the i-th embedded actuator, respectively.

The sensitivities of the topology description functions with respect to the location parameters $c_{ik} \in \left(x_i^0, y_i^0, \theta_i^0\right)$ can be derived from Eqs. (13) and (32) as

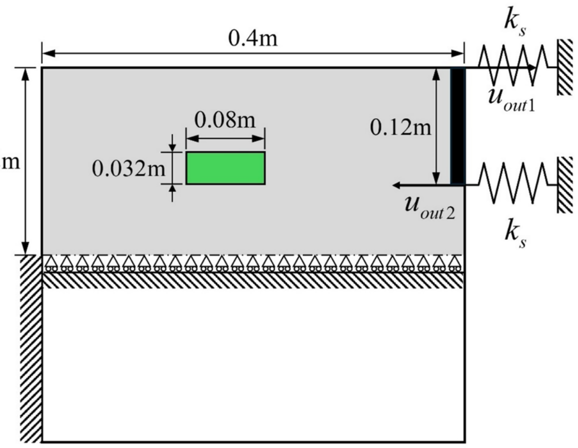

Fig. 8 Analysis domain of the micro-rotation mechanism. The reduced design domain is highlighted in gray

$$\begin{cases} \dfrac{\partial \varphi_i}{\partial x_i^0} = 6\left(\dfrac{\bar{x}_i}{a}\right)^5 \left(\dfrac{-\cos\theta_i^0}{a}\right) + 6\left(\dfrac{\bar{y}_i}{b}\right)^5 \left(\dfrac{\sin\theta_i^0}{b}\right) \\ \dfrac{\partial \varphi_i}{\partial y_i^0} = 6\left(\dfrac{\bar{x}_i}{a}\right)^5 \left(\dfrac{-\sin\theta_i^0}{a}\right) + 6\left(\dfrac{\bar{y}_i}{b}\right)^5 \left(\dfrac{-\cos\theta_i^0}{b}\right) \\ \dfrac{\partial \varphi_i}{\partial \theta_i^0} = 6\left(\dfrac{\bar{x}_i}{a}\right)^5 \left(\dfrac{-\sin\theta_i^0\left(x - x_i^0\right) + \cos\theta_i^0\left(y - y_i^0\right)}{a}\right) \\ +6\left(\dfrac{\bar{y}_i}{b}\right)^5 \left(\dfrac{-\cos\theta_i^0\left(x - x_i^0\right) - \sin\theta_i^0\left(y - y_i^0\right)}{b}\right) \end{cases}. \tag{33}$$

The sensitivity of the fundamental frequency constraint with respect to the design variable s (ζ_i, $\mathbf{c}_i$) can be obtained as

$$\frac{\partial g_3}{\partial s} = \left[\sum_{j=1}^{J_0} \frac{1}{\lambda_j^p}\right]^{-1-\frac{1}{p}} \cdot \left[\sum_{j=1}^{J_0} \frac{1}{\lambda_j^{p+1}} \frac{\partial \lambda_j}{\partial s}\right], \tag{34}$$

where the derivative term $\partial \lambda_j / \partial s$ can be obtained as follows:

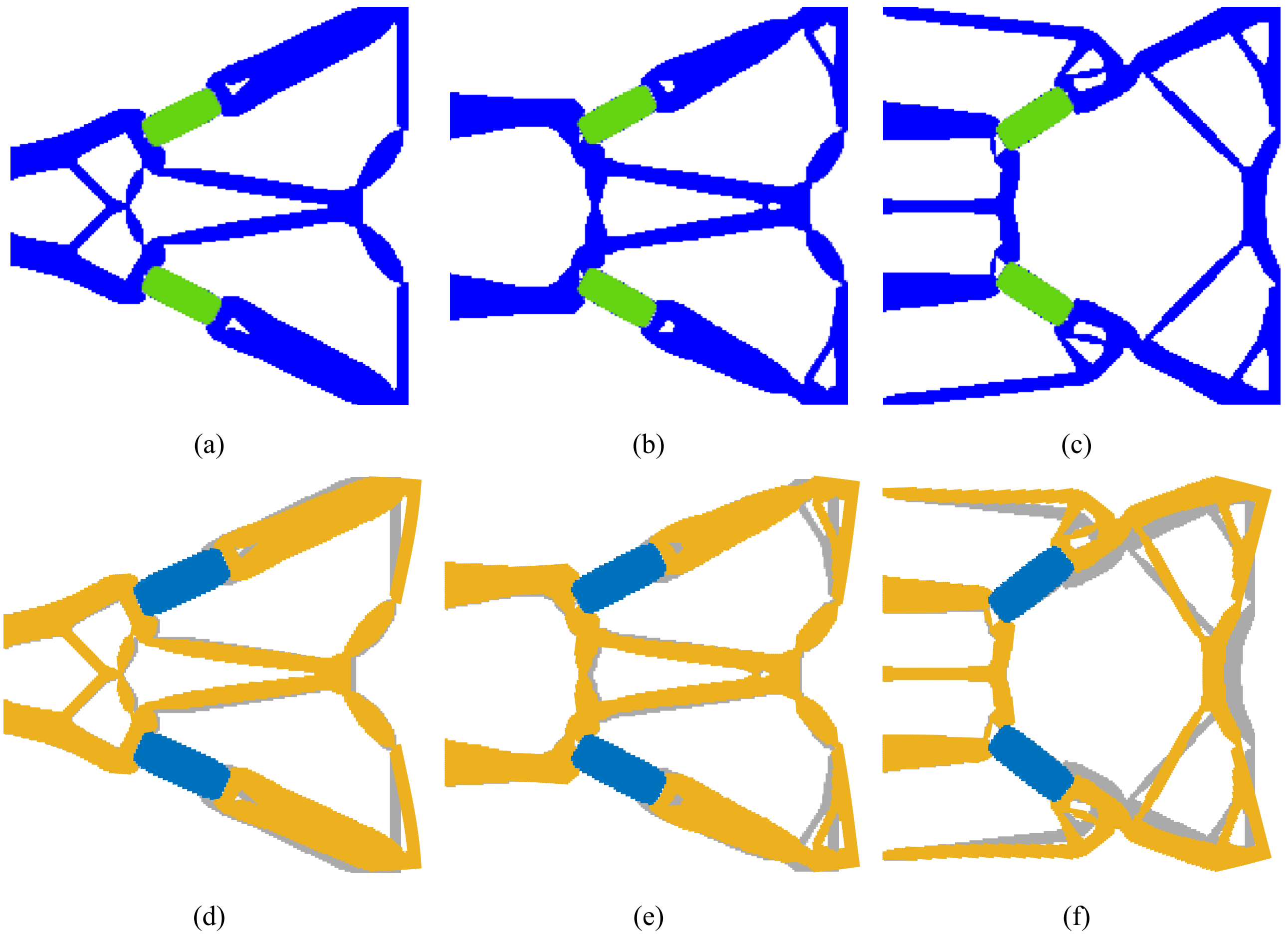

Fig. 9 Optimized topology of the micro-rotation mechanism: **a** without frequency constraint; **b** $\overline{\omega} = 400$ Hz; and **c** $\overline{\omega} = 500$ Hz. Deformation of the optimized designs: **d** without frequency constraint; **e** $\overline{\omega} = 400$ Hz; and **f** $\overline{\omega} = 500$ Hz .

Table 4 Comparing the optimized results for different cases in example 2

	Optimal layout	$f(\mu\text{m})$	ω_1(Hz)	ω_2(Hz)	ω_3(Hz)
No constraint	(0.1720 m, 0.1110 m, –0.4702 rad)	–3.183	255.99	579.06	716.74
$\overline{\omega} = 400$Hz	(0.1683 m, 0.1084 m, –0.5047 rad)	–3.133	400.06	605.99	787.94
$\overline{\omega} = 500$Hz	(0.1528 m, 0.1121 m, –0.5766 rad)	–3.075	500.07	1042.35	1075.62

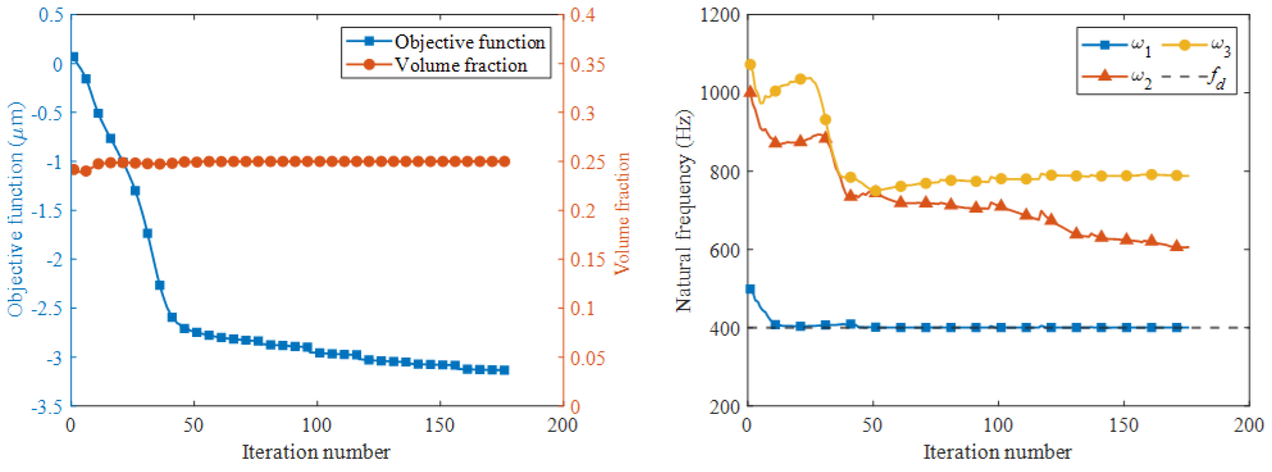

(a) (b)

Fig. 10 Iteration history for $\overline{\omega} = 400$ Hz case: **a** the objective function and volume fraction and **b** the first three eigenfrequencies

$$\frac{\partial \lambda_j}{\partial s} = \boldsymbol{\eta}_j^{\mathrm{T}} \left(\frac{\partial \mathbf{K}_{uu}}{\partial s} - \lambda_j \frac{\partial \mathbf{M}}{\partial s} \right) \boldsymbol{\eta}_j. \tag{35}$$

4 Numerical examples

To verify the effectiveness of the proposed method, three numerical examples are presented in this section. The penalization coefficients of the stiffness matrix and piezoelectric constant matrix are given as $p_1 = 3$ and $p_2 = 4$, respectively, as suggested by Homayouni-Amlashi et al. (2021). The penalization factor of the material density is set to be the same as the stiffness matrix, namely $q = 3$, to prevent localized modes during optimization (Torii and Faria 2017). The approximate fundamental frequency constraint is evaluated by taking three smallest eigenvalues, that is, $J_0 = 3$. The material properties of the piezoelectric actuators used in all examples are given in Table 1. The thickness of the structure is $h = 1.5 \times 10^{-4}$m. In all examples, the initial values of the design variables $\boldsymbol{\zeta}$ are set equal to the volume fraction f_1. The normalized excitation voltage of the piezoelectric actuators is set as 1, and the corresponding actual voltage is 108 V. A specific normalized spring stiffness $\overline{k}_s$ is predefined at the output end of the structure, and the actual value of which can be calculated as follows: $k_s = \overline{k}_s \cdot k_0$, where in all numerical examples $k_0 = 5.489 \times 10^6$ N/m. To avoid checkerboard patterns and obtain black-and-white solutions, a PDE filter and a Heaviside projection filter are applied (Andreassen et al. 2011). The filter radius $R_{\min}$ of the PDE filter is three times the element size. The initial parameter of the Heaviside projection filter β_h is set as 1 for the first 100 iterations and then updates $\beta_h = \min\left(2 * \beta_h, 32\right)$ for every 100 iteration steps or when the change in the objective function is no more than 0.01. The parameter β in Eq. (14) is initially set as 16, and when β_h is greater than β, β is set equal to β_h.

The optimization terminates when the change in the objective function is less than 0.01 or the number of loop steps exceed 300. The method of moving asymptotes (MMA) (Svanberg 2007) is adopted to update design variables for all numerical examples.

4.1 Displacement inverting mechanism

In the first example, a displacement inverting mechanism is studied. The size of the analysis domain is 0.4 m × 0.4 m. To enforce symmetry of design about the horizontal axis, the design domain is selected to be the upper half of the analysis domain, as illustrated in gray in Fig. 3. The size of the rectangular actuators is 0.08m × 0.032m. The analysis domain is discretized using 200 × 200 bilinear quadrilateral plane stress elements. The initial position and orientation

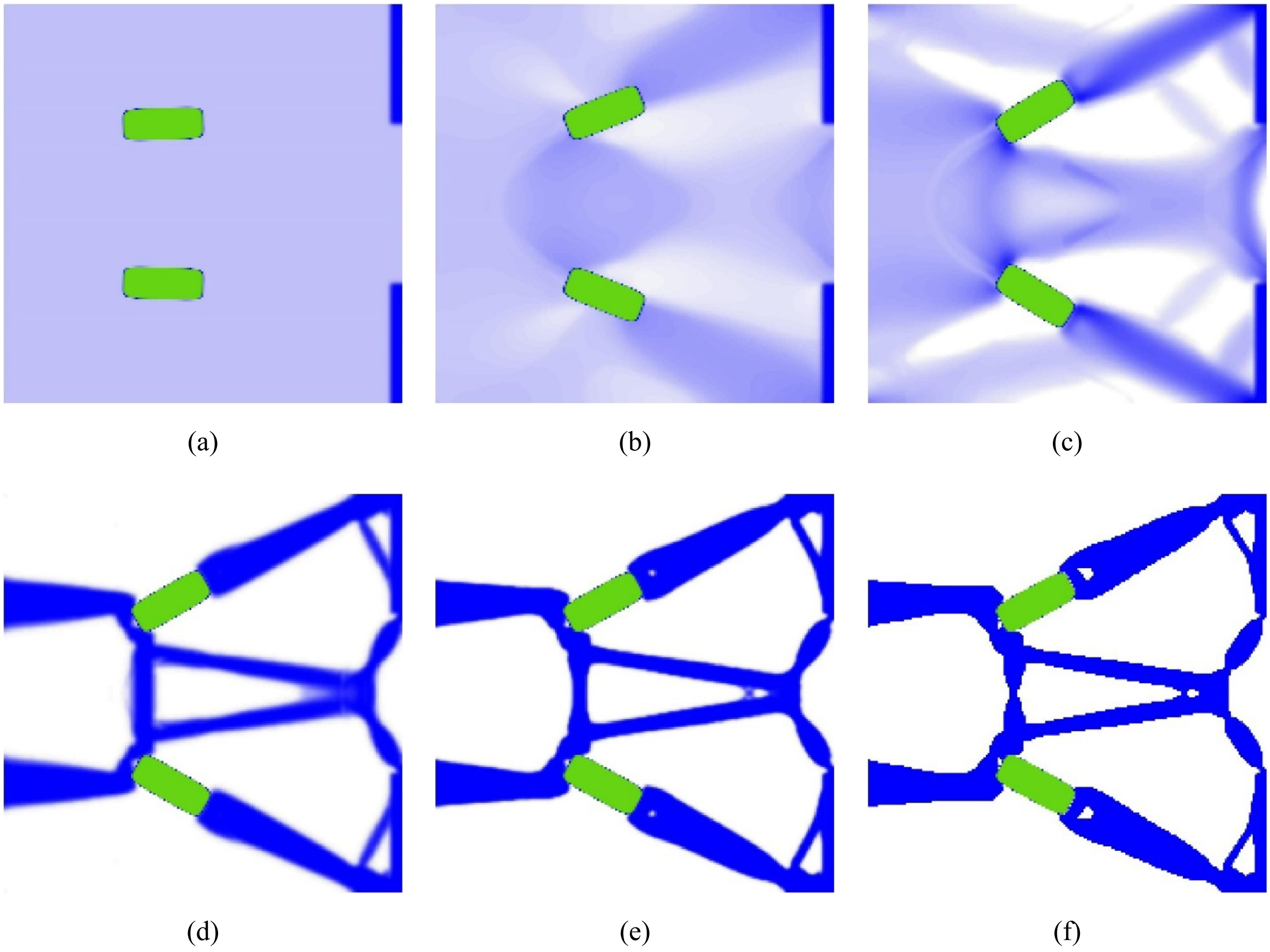
(a) (b) (c)

(d) (e) (f)

Fig. 11 Optimization process of the micro-rotation mechanism under $\overline{\omega} = 400$ Hz: **a** step 1; **b** step 10; **c** step 25; **d** step 50; **e** step 100; and **f** final design

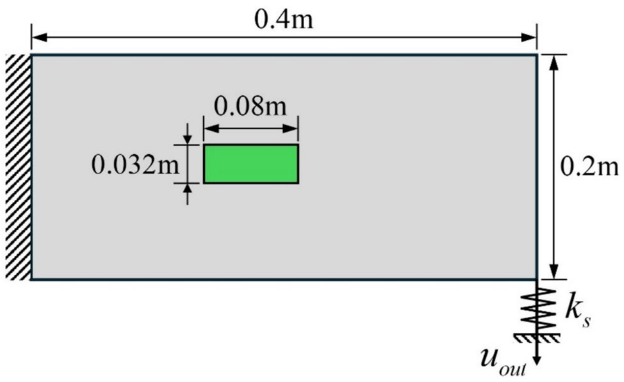

Fig. 12 Design domain of the cantilever compliant mechanism

of the actuator is (0.16 m, 0.12 m, 0 rad). The material of the host structures is aluminum alloy with Young's modulus $E_h = 70$ GPa, Poisson's ratio $\upsilon_h = 0.3$, and density $\rho_h = 2800$ kg/m^3. The volume fraction is set to be $f_1 = 0.2$.

Firstly, the topology optimization model of maximizing the output displacement without fundamental frequency constraint is solved. The optimal result and the deformation under the normalized spring stiffness $\overline{k}_s = 0.005$ are shown in Fig. 4) and d, respectively. The optimal solutions, the objective function, and the first three eigenfrequencies are listed in the first row of Table 2. The rectangle green part in Fig. 4a–c represents the piezoelectric actuator, and the blue part represents the host structure. The first three eigenmodes of the optimized structure are illustrated in Fig. 6a–c.

Next, the influence of the fundamental frequency constraint is investigated by setting $\overline{\omega} = 200$ Hz and $\overline{\omega} = 300$ Hz. The optimal topologies and corresponding solutions are given in Fig. 4b–c and Table 2. The results indicate that adding the fundamental frequency constraint leads to an increase in the host structure connected to the fixed boundary, while the position of the embedded actuators undergoes only minor changes. In addition, with the increase of the upper bound of the fundamental frequency constraint, the output displacement decreases. The iteration history of

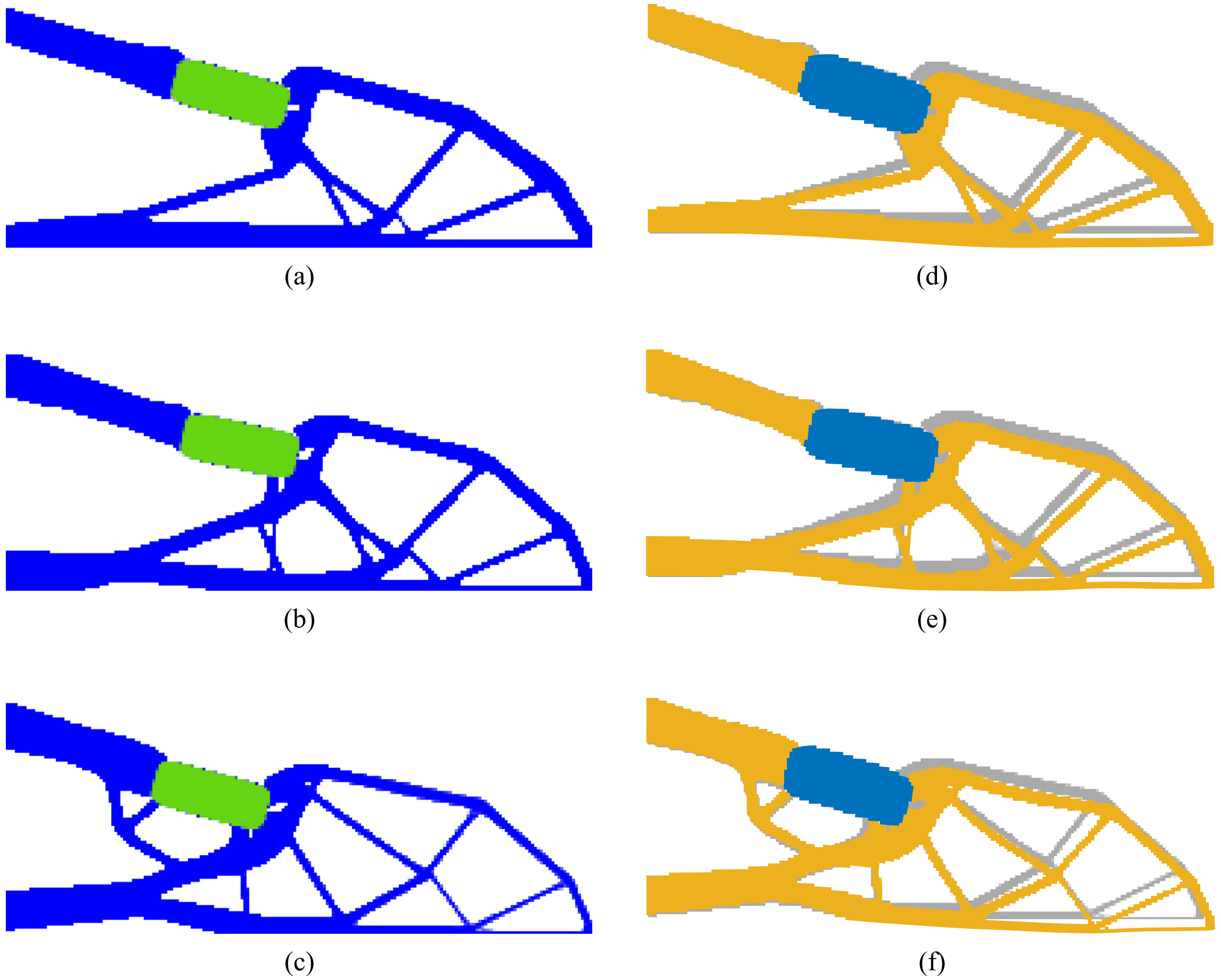

Fig. 13 Optimized topology of the cantilever compliant mechanism with single-embedded actuator: **a** without frequency constraint; **b** $\overline{\omega} = 800$ Hz ; and **c** $\overline{\omega} = 1000$ Hz. Deformation of the optimized designs: **d** without frequency constraint; **e** $\overline{\omega} = 800$ Hz ; and **f** $\overline{\omega} = 1000$ Hz.

Table 5 Comparing the optimized results for different cases in example 3

	Optimal layout	$u_{\text{out}}(\mu m)$	ω_1(Hz)	ω_2(Hz)	ω_3(Hz)
No constraint	(0.1532 m, 0.0945 m, 0.2697 rad)	–2.686	627.04	1152.58	1357.62
$\overline{\omega} = 800$ Hz	(0.1596 m, 0.1005 m, 0.2082 rad)	–2.551	800.10	1259.26	2117.43
$\overline{\omega} = 1000$ Hz	(0.1397 m, 0.1048 m, 0.2632 rad)	–2.465	1000.03	1713.45	2214.92

the displacement inverting mechanism under $\overline{\omega} = 300$ Hz is plotted in Fig. 5. It is seen that the fundamental frequency achieved convergence within 30 iteration steps, which verifies the efficiency of the proposed method. Figure 6d–f depicts the first three eigenmodes of the optimized structure with fundamental frequency constraint $\overline{\omega} = 300$ Hz. It is seen that all of these eigenmodes are global deformations, and no local modes exist.

Furthermore, the optimization process is proposed under different output spring stiffness. The optimal designs for $\overline{k}_s = 0.01$, $\overline{k}_s = 0.05$, and $\overline{k}_s = 0.1$ are illustrated in Fig. 7, and optimal solutions, objective function, and the fundamental frequencies are listed in Table 3. The results indicate that a larger spring stiffness leads to a stiffer design with thicker connection beams and results in a larger fundamental frequency and smaller output displacement.

4.2 Micro-rotation mechanism

In the second example, a micro-rotation mechanism is optimized using the proposed method. As shown in Fig. 8, the optimization objective is to generate two equal-sized,

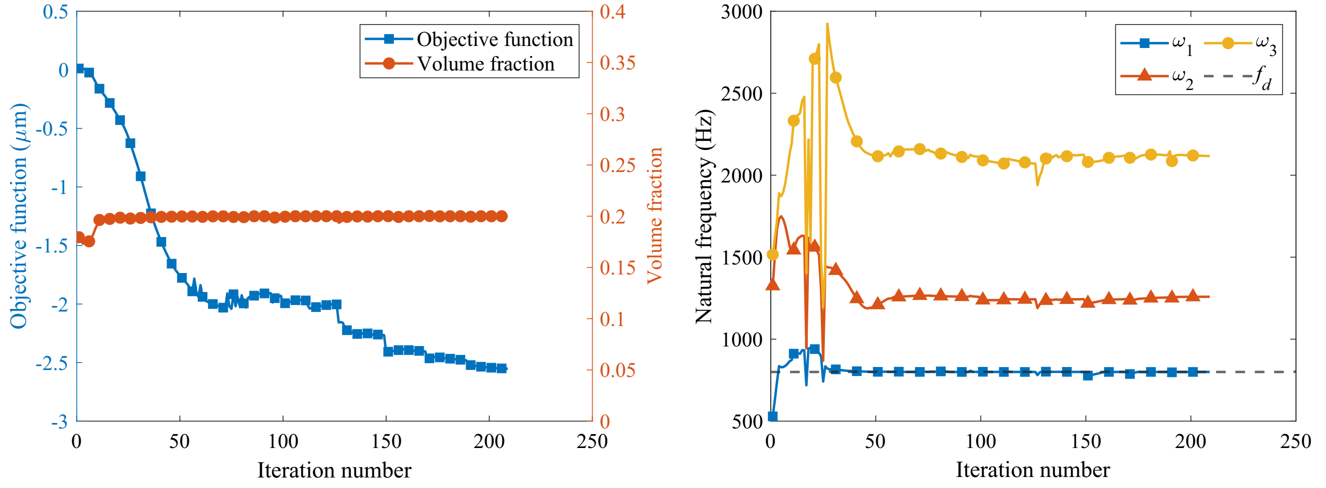

(a) (b)

Fig. 14 Iteration history of for $\overline{\omega} = 800$ Hz case: **a** The objective function and volume fraction and **b** the first three eigenfrequencies

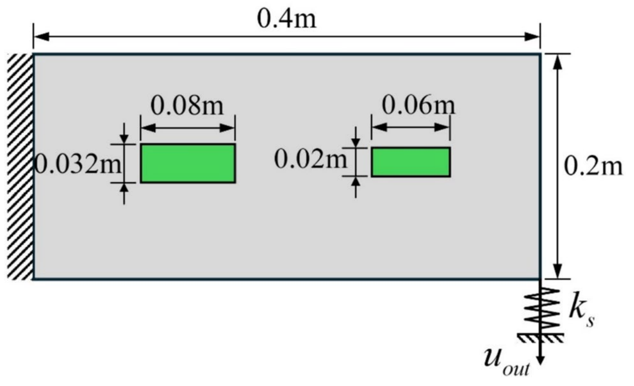

Fig. 15 Design domain of the cantilever compliant mechanism with two embedded actuators

oppositely directed angles or torques at the upper-right and lower-right corners. Thus, the objective function of this example can be expressed as follows: max $\left(f = u_{\text{out1}} - u_{\text{out2}}\right)$. The size of the analysis domain is $0.4\text{m} \times 0.4\text{m}$. The analysis domain is discretized using 200×200 bilinear quadrilateral plane stress elements. To enforce symmetry of design about the horizontal axis, the design domain is selected to be the upper half of the analysis domain.

The material of the host structures is aluminum alloy with Young's modulus $E_{\text{h}} = 70\text{GPa}$, Poisson's ratio $\upsilon_{\text{h}} = 0.3$, and density $\rho_{\text{h}} = 2800\text{kg/m}^3$. The volume fraction is set to be $f_1 = 0.25$. The normalized spring stiffness at the output port is set to be $\overline{k}_s = 0.1$ in this example. The initial layout of the embedded actuators and remaining geometric parameters are the same as those in the previous example.

Firstly, the topology optimization model without fundamental frequency constraint is solved. The optimized design and its deformed shape are shown in Fig. 9a and d, respectively. The optimal layout of the embedded actuator, objective function, and the first three eigenfrequencies of the optimized design are listed in the first row of Table 4. Next, the topology optimization is implemented considering fundamental frequency constraints $\overline{\omega} = 400$ Hz and $\overline{\omega} = 500$ Hz. The optimal topologies and their deformed shape and the corresponding solutions are given in Fig. 9b–c, e–f and Table 4. It can be observed that the optimized topologies of the three cases exhibit significant differences, while the deformation mode of which remain unchanged. The iteration curves of the objective function and first three frequencies for $\overline{\omega} = 400$ Hz are shown in Fig. 10. The small oscillations of the iteration curves are mainly caused by the updates of the sharpness parameters β_h. Several intermediate designs are illustrated in Fig. 11, which indicate that the actuator location is updated at the beginning of the optimization process, after that, the topology of the host structure is generated. The above results proved that the smoothed fundamental frequency constraint function proposed in this study could effectively control the fundamental frequency of the piezo-embedded structure, which verified the effectiveness of the presented optimization framework.

4.3 Cantilever compliant mechanism

In this section, a cantilever compliant mechanism with a single-embedded actuator is considered. The design domain of this cantilever compliant mechanism is shown in Fig. 12. The optimization objective of this example is to maximize the vertical output displacement against the y-direction at the right bottom corner. The size of the analysis domain is

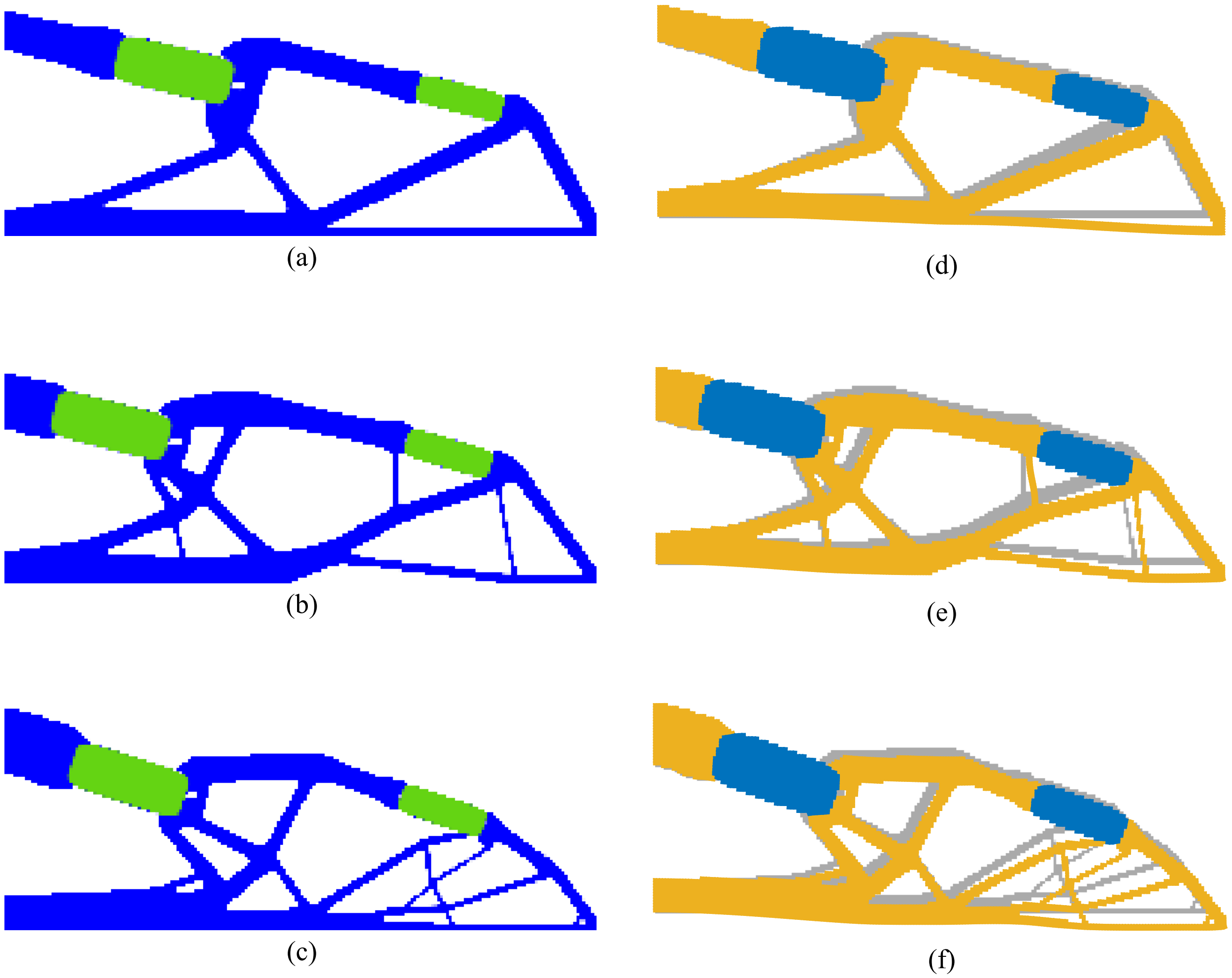

Fig. 16 Optimized topology of the cantilever compliant mechanism with two embedded actuators: **a** without frequency constraint; **b** $\overline{\omega} = 750$ Hz; and **c** $\overline{\omega} = 850$ Hz . Deformation of the optimized designs: **a** without frequency constraint; **b** $\overline{\omega} = 750$ Hz ; and **c** $\overline{\omega} = 850$ Hz

Table 6 Comparing the optimized results for different cases in example 4

	Optimal layout	Optimal layout	$u_{\text{out}}(\mu\text{m})$	ω_1(Hz)
No constraint	(0.1144 m, 0.0876 m, 0.2346 rad)	(0.3077 m, 0.1066 m, 0.2561 rad)	–3.760	667.31
$\overline{\omega} = 750$ Hz	(0.0721 m, 0.0931 m, 0.2472 rad)	(0.2999 m, 0.1120 m, 0.2920 rad)	–3.583	750.12
$\overline{\omega} = 850$ Hz	(0.0838 m, 0.0979 m, 0.3146 rad)	(0.2957 m, 0.1188 m, 0.3276 rad)	–3.409	850.03

0.4 m × 0.2 m. The size and the initial layout of the embedded actuators are 0.08 m × 0.032 m and (0.16m, 0.11m, 0rad), respectively. The analysis domain is discretized using 200 × 100 bilinear quadrilateral plane stress elements. The material of the host structures is structural steel with Young's modulus $E_{\text{h}} = 200$ GPa, Poisson's ratio $\upsilon_{\text{h}} = 0.3$, and density $\rho_{\text{h}} = 7850\ \text{kg/m}^3$. The volume fraction is set to be $f_1 = 0.2$. The normalized spring stiffness at the output port is set to be $\overline{k}_s = 0.1$ in this example.

The cases without a fundamental frequency constraint and with $\overline{\omega} = 800$ Hz and $\overline{\omega} = 1000$ Hz fundamental frequency constraint are optimized, respectively. The optimized designs and their deformed shapes are shown in Fig. 13, and the optimal layout of the embedded actuator, objective function, and the first three eigenfrequencies are listed in Table 5. The iteration curves of the cantilever compliant mechanism under $\overline{\omega} = 800$ Hz are shown in Fig. 14.

To further validate the proposed optimization method, the optimization is also presented with different sizes and number of embedded actuators. In this case, a cantilever compliant mechanism with two embedded actuators is

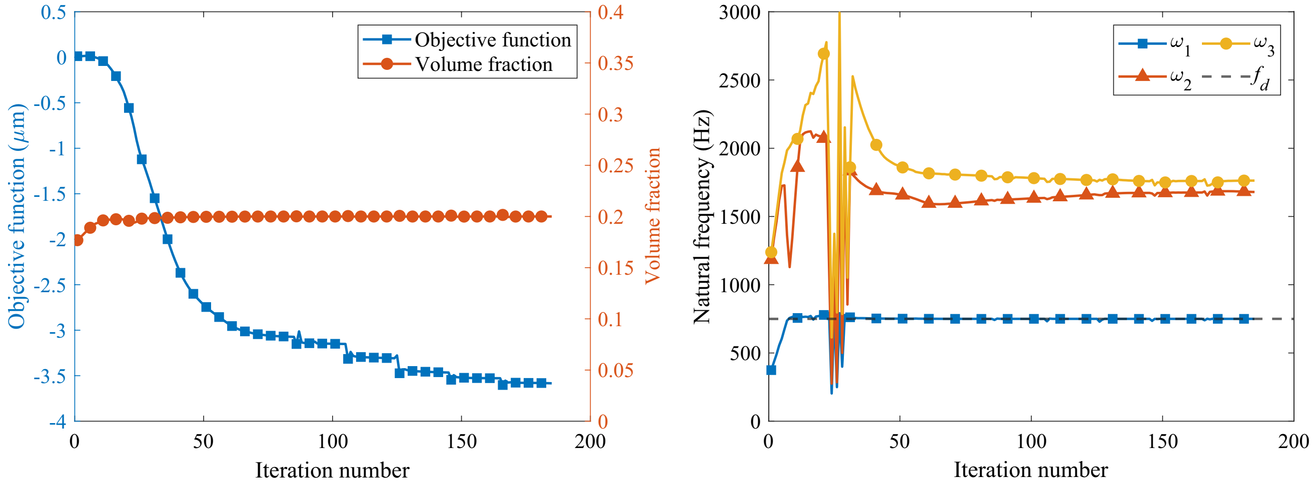

(a) (b)

Fig. 17 Iteration history of for $\overline{\omega} = 750$ Hz case: **a** the objective function and volume fraction and **b** the first three eigenfrequencies

considered, as illustrated in Fig. 15. The actuators with sizes 0.08m × 0.032 m and 0.06m × 0.02 m are located at (0.11 m, 0.11 m, 0 rad) and (0.31 m, 0.11 m, 0 rad), respectively. Other parameters are the same as those in the previous example.

The cases with no fundamental frequency constraint and $\overline{\omega} = 750$ Hz, $\overline{\omega} = 850$ Hz fundamental frequency constraint are optimized, respectively. The optimized designs and their deformed shapes are shown in Fig. 16, and the optimal layout of the embedded actuator, objective function, and the first three eigenfrequencies are listed in Table 6. The iteration curves under $\overline{\omega} = 750$ Hz are shown in Fig. 17.

5 Conclusion

This paper presents a concurrent optimization method of compliant structures embedded with movable piezoelectric actuators considering fundamental frequency constraints. In this approach, the layout of compliant mechanisms and piezoelectric actuators is simultaneously optimized by employing a SIMP-based computational framework. More specifically, the geometry and location of the embedded actuators described by a K–S function are mapped into a density field, which ensures computational efficiency by avoiding the need for remeshing the grid. To overcome the non-differentiability issue, a p-norm approximation function is employed for the fundamental frequency constraint. Sensitivities of objective and constraints are derived using the adjoint method and the optimization problem is solved using the gradient-based optimizer. Numerical examples are investigated to verify the effectiveness of the proposed method. The iteration curves of the objective and constraints demonstrate that the proposed method is differentiable and stable, and clear topologies of embedded actuators and the host structure can be obtained for all examples, which preliminarily validate the effectiveness of the proposed method. It is also seen that the fundamental frequency constraints are well satisfied, and no local modes exist. The optimized designs of the piezo-actuated compliant mechanism considering fundamental frequency constraints are significantly different from the designs without frequency constraints, which demonstrates the necessity of considering dynamics properties when designing compliant mechanisms.

Acknowledgements This work is supported by the National Natural Science Foundation of China (Grant Nos. 12272076, U2341232 and 11821202) and the 111 Project (B14013).

Declarations

Conflict of interest The authors declare that they have no conflicts of interest.

Replication of results The results provided in this paper can be reproduced by the implementation details provided herein. The MATLAB codes developed in this study are available on request from the corresponding author.

References

Allaire G, Jouve F, Toader AM (2004) Structural optimization using sensitivity analysis and a level-set method. J Comput Phys 194:363–393. https://doi.org/10.1016/j.jcp.2003.09.032

Andreassen E, Clausen A, Schevenels M, Lazarov BS, Sigmund O (2011) Efficient topology optimization in MATLAB using 88 lines of code. Struct Multidisc Optim 43:1–16. https://doi.org/10.1007/s00158-010-0594-7

Ansola R, Veguería E, Canales J, Tárrago JA (2007) A simple evolutionary topology optimization procedure for compliant mechanism design. Fin Elem Anal Des 44:53–62. https://doi.org/10.1016/j.finel.2007.09.002

Bendsøe MP, Kikuchi N (1988) Generating optimal topologies in structural design using a homogenization method. Comput Methods Appl Mech Eng 71(2):197–224. https://doi.org/10.1016/0045-7825(88)90086-2

Clark L, Shirinzadeh B, Pinskier J, Tian Y, Zhang D (2018) Topology optimisation of bridge input structures with maximal amplification for design of flexure mechanisms. Mech Mach Theory 122:113–131. https://doi.org/10.1016/j.mechmachtheory.2017.12.017

da Silva GA, Beck AT, Sigmund O (2019) Topology optimization of compliant mechanisms with stress constraints and manufacturing error robustness. Comput Methods Appl Mech Eng 354:397–421. https://doi.org/10.1016/j.cma.2019.05.046

Du J, Olhoff N (2007) Topological design of freely vibrating continuum structures for maximum values of simple and multiple eigenfrequencies and frequency gaps. Struct Multidiscip Optim 34:91–110. https://doi.org/10.1007/s00158-007-0101-y

Gao J, Xiao M, Yan Z, Gao L, Li H (2022) Robust isogeometric topology optimization for piezoelectric actuators with uniform manufacturability. Front Mech Eng 17(2):27. https://doi.org/10.1007/s11465-022-0683-5

Gao J, Cao X, Xiao M, Yang Z, Zhou X, Li Y, Gao L, Yan W, Rabczuk T, Mai Y-W (2023) Rational designs of mechanical metamaterials: formulations, architectures, tessellations and prospects. Mater Sci Eng R Rep 156:100755. https://doi.org/10.1016/j.mser.2023.100755

Gravesen J, Evgrafov A, Nguyen DM (2011) On the sensitivities of multiple eigenvalues. Struct Multidiscip Optim 44:583–587. https://doi.org/10.1007/s00158-011-0644-9

Guo X, Zhang W, Zhong W (2014) Doing topology optimization explicitly and geometrically-a new moving morphable components based framework. J Appl Mech 81:081009–081012. https://doi.org/10.1115/1.4027609

Hoang VN, Jang GW (2017) Topology optimization using moving morphable bars for versatile thickness control. Comput Methods Appl Mech Eng 317:153–173. https://doi.org/10.1016/j.cma.2016.12.004

Homayouni-Amlashi A, Schlinquer T, Mohand-Ousaid A, Rakotondrabe M (2021) 2D topology optimization MATLAB codes for piezoelectric actuators and energy harvesters. Struct Multidiscip Optim 63:983–1014. https://doi.org/10.1007/s00158-020-02726-w

Hu J, Liu Y, Huang H, Liu S (2024a) Integrated optimization of components' layout and structural topology with considering the interface stress constraint. Comput Methods Appl Mech Eng 419:116588. https://doi.org/10.1016/j.cma.2023.116588

Hu J, Wallin M, Ristinmaa M, Liu Y, Liu S, (2024b) Integrated multi-material and multi-scale optimization of compliant structure with embedded movable piezoelectric actuators. Comput Methods Appl Mech Eng 421:116786. https://doi.org/10.1016/j.cma.2024.116786

Huang X, Xie YM (2007) Convergent and mesh-independent solutions for the bi-directional evolutionary structural optimization method. Fin Elem Anal Des 43:1039–1049. https://doi.org/10.1016/j.finel.2007.06.006

Kögl M, Silva EC (2005) Topology optimization of smart structures: design of piezoelectric plate and shell actuators. Smart Mater Struct 14:387–399. https://doi.org/10.1088/0964-1726/14/2/013

Lai J, Yu L, Yuan L, Liang J, Ling M, Wang R, Zang H, Li H, Zhu B, Zhang X (2023) An integrated modeling method for piezo-actuated compliant mechanisms. Sens Actuators A Phys 364:114770. https://doi.org/10.1016/j.sna.2023.114770

Leader MK, Chin TW, Kennedy GJ (2019) High-resolution topology optimization with stress and natural frequency constraints. AIAA J 57:3562–3578. https://doi.org/10.2514/1.J057777

Li B, Ding S, Guo S, Su W, Cheng A, Hong J (2021) A novel isogeometric topology optimization framework for planar compliant mechanisms. Appl Math Model 92:931–950. https://doi.org/10.1016/j.apm.2020.11.032

Li B, Fu Y, Kennedy GJ (2023) Topology optimization using an eigenvector aggregate. Struct Multidiscip Optim 66:221. https://doi.org/10.1007/s00158-023-03674-x

Ling M (2019) A general two-port dynamic stiffness model and static/dynamic comparison for three bridge-type flexure displacement amplifiers. Mech Syst Signal Process 119:486–500. https://doi.org/10.1016/j.ymssp.2018.10.007

Liu M, Zhan J, Zhu B, Zhang X (2020) Topology optimization of compliant mechanism considering actual output displacement using adaptive output spring stiffness. Mech Mach Theory 146:103728. https://doi.org/10.1016/j.mechmachtheory.2019.103728

Lobontiu N, Garcia E (2003) Analytical model of displacement amplification and stiffness optimization for a class of flexure-based compliant mechanisms. Comput Struct 81:2797–2810. https://doi.org/10.1016/j.compstruc.2003.07.003

Lopes HN, Mahfoud J, Pavanello R (2021) High natural frequency gap topology optimization of bi-material elastic structures and band gap analysis. Struct Multidiscip Optim 63:2325–2340. https://doi.org/10.1007/s00158-020-02811-0

Luo Z, Tong L, Luo J, Wei P, Wang MY (2009) Design of piezoelectric actuators using a multiphase level set method of piecewise constants. J Comput Phys 228:2643–2659. https://doi.org/10.1016/j.jcp.2008.12.019

Luo Z, Gao W, Song C (2010) Design of multi-phase piezoelectric actuators. J Intell Mater Syst Struct 21:1851–1865. https://doi.org/10.1177/1045389X10389345

Ma Z, Cheng H, Kikuchi N (1994) Structural design for obtaining desired eigenfrequencies by using the topology and shape optimization method. Comput Syst Eng 5:77–89

Maddisetty H, Frecker M (2004) Dynamic topology optimization of compliant mechanisms and piezoceramic actuators. J Mech Des 126:975–983. https://doi.org/10.1115/1.1814638

Mallick R, Ganguli R, Bhat MS (2014) A feasibility study of a post-buckled beam for actuating helicopter trailing edge flap. Acta Mech 225:2783–2787. https://doi.org/10.1007/s00707-014-1215-0

Moore SI, Yong YK, Omidbeike M, Fleming AJ (2021) Serial-kinematic monolithic nanopositioner with in-plane bender actuators. Mechatronics 75:102541. https://doi.org/10.1016/j.mechatronics.2021.102541

Nishiwaki S, Frecker MI, Min S, Kikuchi N (1998) Topology optimization of compliant mechanisms using the homogenization method. Int J Numer Methods Eng 42(3):535–559. https://doi.org/10.1002/(SICI)1097-0207(19980615)42:3%3c535::AID-NME372%3e3.0.CO;2-J

Pedersen CB, Buhl T, Sigmund O (2001) Topology synthesis of large-displacement compliant mechanisms. Int J Numer Meth Eng 50(12):2683–2705. https://doi.org/10.1002/nme.148

Quinteros L, Meruane V, Cardoso EL (2021) Phononic band gap optimization in truss-like cellular structures using smooth P-norm approximations. Struct Multidiscip Optim 64:113–124. https://doi.org/10.1007/s00158-021-02862-x

Schmerbauch AEM, Vasquez-Beltran MA, Vakis AI, Huisman R, Jayawardhana B (2020) Influence functions for a hysteretic deformable mirror with a high-density 2D array of actuators. Appl Opt 59:8077–8088. https://doi.org/10.1364/ao.397472

Seyraniant AP, Lund E, Olhoff N (1994) Multiple eigenvalues in structural optimization problems. Struct Optim 8(4):207–227. https://doi.org/10.1007/BF01742705

Shi B, Wang F, Huo Z, Tian Y, Zhao X, Zhang D (2022) Design of a rhombus-type stick-slip actuator with two driving modes for micropositioning. Mech Syst Signal Process 166:108421. https://doi.org/10.1016/j.ymssp.2021.108421

Sigmund O (1997) On the design of compliant mechanisms using topology optimization. Mech Struct Mach 25:493–524. https://doi.org/10.1080/08905459708945415

Sun J, Guan Q, Liu Y, Leng J (2016) Morphing aircraft based on smart materials and structures: a state-of-the-art review. J Intell Mater Syst Struct 27:2289–2312. https://doi.org/10.1177/1045389X1662956

Svanberg K (2007) MMA and GCMMA–two methods for nonlinear optimization. Available for download at https://people.kth.se/krille/mmagcmma.pdf

Teimouri M, Asgari M (2019) Multi-objective BESO topology optimization for stiffness and frequency of continuum structures. Struct Eng Mech 72:181–190. https://doi.org/10.12989/sem.2019.72.2.181

Torii AJ, Faria JR (2017) Structural optimization considering smallest magnitude eigenvalues: a smooth approximation. J Braz Soc Mech Sci Eng 39:1745–1754. https://doi.org/10.1007/s40430-016-0583-x

Van Dijk NP, Maute K, Langelaar M, Van Keulen F (2013) Level-set methods for structural topology optimization: a review. Struct Multidiscip Optim 48:437–472

Wang MY, Wang X, Guo D (2003) A level set method for structural topology optimization. Comput Methods Appl Mech Eng 192(1-2):227–246. https://doi.org/10.1016/S0045-7825(02)00559-5

Wang MY, Chen S, Wang X, Mei Y (2005) Design of multimaterial compliant mechanisms using level-set methods. J Mech Des 127:941–956. https://doi.org/10.1115/1.1909206

Wang Y, Luo Z, Zhang X, Kang Z (2014) Topological design of compliant smart structures with embedded movable actuators. Smart Mater Struct 23:045024. https://doi.org/10.1088/0964-1726/23/4/045024

Wang G, Yan Y, Ma J, Cui J (2019) Design, test and control of a compact piezoelectric scanner based on a compound compliant amplification mechanism. Mech Mach Theory 139:460–475. https://doi.org/10.1016/j.mechmachtheory.2019.05.009

Wang X, Hu P, Kang Z (2020) Layout optimization of continuum structures embedded with movable components and holes simultaneously. Struct Multidiscip Optim 61:555–573. https://doi.org/10.1007/s00158-019-02378-5

Wang R, Zhang X, Zhu B, Qu F, Chen B, Liang J (2022) Hybrid explicit–implicit topology optimization method for the integrated layout design of compliant mechanisms and actuators. Mech Mach Theory 171:104750. https://doi.org/10.1016/j.mechmachtheory.2022.104750

Wang M, Zhang C, Liu S, Wang X (2023) Modeling and analysis of a conical bridge-type displacement amplification mechanism using the non-uniform rational B-spline curve. Materials 16:6162. https://doi.org/10.3390/ma16186162

Zhang W, Li D, Kang P, Guo X, Youn S-K (2020) Explicit topology optimization using IGA-based moving morphable void (MMV) approach. Comput Methods Appl Mech Eng 360:112685. https://doi.org/10.1016/j.cma.2019.112685

Zhu B, Zhang X (2012) A new level set method for topology optimization of distributed compliant mechanisms. Int J Numer Methods Eng 91:843–871. https://doi.org/10.1002/nme.4296

Zhu B, Zhang X, Zhang H, Liang J, Zang H, Li H, Wang R (2020) Design of compliant mechanisms using continuum topology optimization: a review. Mech Mach Theory 143:103622. https://doi.org/10.1016/j.mechmachtheory.2019.103622

Zhu B, Wang R, Wang N, Li H, Zhang X, Nishiwaki S (2021) Explicit structural topology optimization using moving wide Bezier components with constrained ends. Struct Multidiscip Optim 64:53–70. https://doi.org/10.1007/s00158-021-02853-y